# Electroactive ZnO: Mechanisms, Conductivity, and Advances in Zn Alkaline Battery Cycling

*Brendan E. Hawkins, Damon E. Turney*, Robert J. Messinger, Andrew M. Kiss, Gautam G. Yadav, Sanjoy Banerjee, Timothy N. Lambert*

B. E. Hawkins, D. E. Turney, R. J. Messinger, G. G. Yadav, S. Banerjee
Department of Chemical Engineering, The City College of New York, 160 Convent Avenue, New York, New York 10031, United States
E-mail: damonturney@gmail.com, dturney@ccny.cuny.edu

A. M. Kiss
National Synchrotron Light Source II, Brookhaven National Laboratory, Upton, New York 11973, United States

T. N. Lambert
Department of Photovoltaics and Materials Technologies, Sandia National Laboratories PO Box 5800, Albuquerque, New Mexico 87185, United States

Keywords: zinc oxide, zinc, alkaline, battery, electrochromism, passivation, sustainability

Zinc oxide (ZnO) is of great interest for advanced energy devices because of its low cost, wide direct band gap, non-toxicity, and facile electrochemistry. In zinc (Zn) alkaline batteries, ZnO plays a critical role in electrode passivation, a process that hinders commercialization and remains poorly understood. Here, we disclose novel observations of an electroactive type of ZnO formed in Zn-metal alkaline electrodes. We measure the electrical conductivity of battery-formed ZnO to vary by factors of up to $10^4$, which provides a first-principles-based understanding of Zn passivation in industrial alkaline batteries. Simultaneous with this conductivity change, protons are inserted into the crystal structure and electrons are inserted into the conduction band in quantities up to ~$10^{20}$ $cm^{-3}$ and ~1 $mAh/g_{ZnO}$. Electron insertion causes blue electrochromic coloration with efficiencies and rates competitive with leading electrochromic materials. The electroactivity of ZnO is evidently enabled by rapid crystal growth, which forms defects that

complex with inserted cations, charge-balanced by the increase of conduction band electrons. This property distinguishes electroactive ZnO from inactive classical ZnO. We apply knowledge of this phenomenon to improve cycling performance of industrial-design electrodes at 50% zinc utilization and propose other uses for ZnO such as electrochromic devices.

## 1. Introduction

Zinc oxide (ZnO) is of significant interest to next-generation energy systems and is studied extensively for many technologies such as (i) rechargeable zinc alkaline batteries,[1,2,3,4] (ii) transparent front-contacts on thin-film solar cells and electrochromic windows,[5,6] (iii) semiconductor lighting and switching,[7,8] and (iv) catalysts for solar energy conversion and water splitting. [9,10] Despite this widespread interest, commercialization of devices based on ZnO has been limited due to difficulty controlling its electronic properties in part due to an incomplete understanding or control of the effects of doping and native defects. [7] A better understanding of the origins of these properties must be developed to promote the commercialization of ZnO-based devices.

These considerations are particularly important for ZnO in rechargeable zinc (Zn) metal alkaline batteries, abbreviated "Zn alkaline batteries", which are attractive for electric grid integration of renewable energy sources because of the low cost, inherent safety, environmental friendliness, and high energy density of Zn. However, rechargeable Zn alkaline batteries have not yet been widely commercialized due to poor cycle life of zinc anodes at high utilization. Failure analyses show ZnO passivation of Zn metal to be a leading failure mechanism. [1,2,3,11] The exact passivation mechanism of Zn metal by ZnO has stood uncontrolled and unexplained for decades since the first reports of so-called "type I" and "type II" ZnO. [12,13,14,15,16] Recent studies have attempted empirical solutions to the passivation problem by use of Zn sponge architecture,[17] water-in-salt electrolyte,[18] or conductive carbon frameworks,[19] but these improvements often require significant extra costs and increased battery volume, negating key benefits of Zn battery chemistry. The properties, behavior, and effects of the different types of ZnO formed in alkaline batteries are clearly complex, and they must be better understood to improve Zn battery performance.

ZnO used in Zn batteries is historically generated via the indirect (French) process in which Zn metal is vaporized and exposed to oxygen at high temperature (>1000°C) to form wurtzite ZnO. This "classical ZnO" is well-known to have stoichiometric composition, no electrochromic

activity, no electrochemical intercalation capacity, high transparency to infrared and red wavelengths,[20] and resistivity of ~$10^2$ Ω-cm for single-crystals[21] or >$10^8$ Ω-cm for powders.[22]

Recent publications[9,23] show new behavior from ZnO nanocrystals (1 to 10 nm) in organic-solvent dispersions, wherein the nanocrystalline ZnO accommodates coupled insertion of electrons and cations $M^{y+}$ from the electrolyte

(1) $xM^{y+} + xye^- + ZnO_{colorless} \leftrightarrow M_xZnO_{blue}$

causing an increase in ZnO conduction band electrons. This electrochemical reaction is very similar to reactions that occur in well-studied metal oxide "bronzes" such as $WO_3$ and $MoO_3$, where simultaneous cation and electron insertion causes great changes to the color and conductivity of the materials. [24] A great amount of research was accomplished by these researchers on nanocrystalline "electroactive" ZnO, but no characterization or explanation is yet published for why this ZnO is electroactive, but classical ZnO is not. Generation of atomic-scale understanding of crystal structure and reaction mechanisms enabling this novel electrochemical activity would be a valuable step toward future research and development.

Here, we discover that the ZnO that forms in Zn alkaline batteries, which is not nanocrystalline (>100 nm), is this same electroactive ZnO reported in recent literature, and that this electroactive ZnO is the key material governing passivation of industrial Zn alkaline battery anodes through variation of its electrical conductivity by factors up to ~$10^4$. Knowledge of this variable conductivity leads to innovations that improve the performance of industrial-design Zn batteries. Deep materials characterizations, including quantitative solid-state $^1$H magic-angle-spinning (MAS) nuclear magnetic resonance (NMR) spectroscopy and operando confocal Raman spectroscopy, reveal that the crystal growth rate in alkaline electrolyte governs the formation of key defects, which enable electrochemical intercalation of cations from the aqueous electrolyte. In aggregate, this report explains the physical mechanism for the recently discovered ZnO electroactivity and demonstrates how this knowledge can be applied to improve Zn battery performance. We hope these results promote further research on ZnO in batteries and other devices for the development of next-generation energy systems.

## 2. Results and Discussion

### 2.1 Electroactive ZnO formation and Zn passivation in alkaline electrolyte

The prevailing perspective in the alkaline battery community is that battery-formed ZnO is electrochemically inactive and has electrical conductivities similar to classical ZnO, introduced above.[25,26] However, here we report large and controllable variations of the electronic properties of a special type of battery-formed wurtzite ZnO that we name "electroactive" ZnO. A simple demonstration of this electroactivity can be observed by discharging standard industrial-design paste-zinc alkaline electrodes[1,2,3,4] in tight industrial battery boxes with 5.5 M aqueous potassium hydroxide (KOH), at either a fast rate (25 mA $g^{-1}$) or a slow rate (5 mA $g^{-1}$) until 50% of the Zn metal is oxidized. The 25 mA/g discharge, which is a typical rate for battery operation, generates a deep-blue ZnO layer that changes color from blue to white as electrode potential is increased (**Figure 1**a). We show later in this section that this electroactive ZnO hosts electrochemical reactions, and we show in section 2.2 that electroactive ZnO has higher conductivity in the blue state and lower conductivity in the white state. In contrast, the 5 mA/g discharge experiment produces ZnO that is much less reactive electrochemically and is more white in appearance, altogether closer in character to classical ZnO. This dependence of material properties on discharge rate suggests crystal growth rate is the synthesis parameter that differentiates the classical from electroactive ZnO forms, discussed further in section 2.5. The prior publications on nanocrystalline electroactive ZnO also used a hydroxide salt, tetramethylammonium hydroxide, along with zinc acetate to form electroactive ZnO in nonaqueous electrolyte. [9,10]

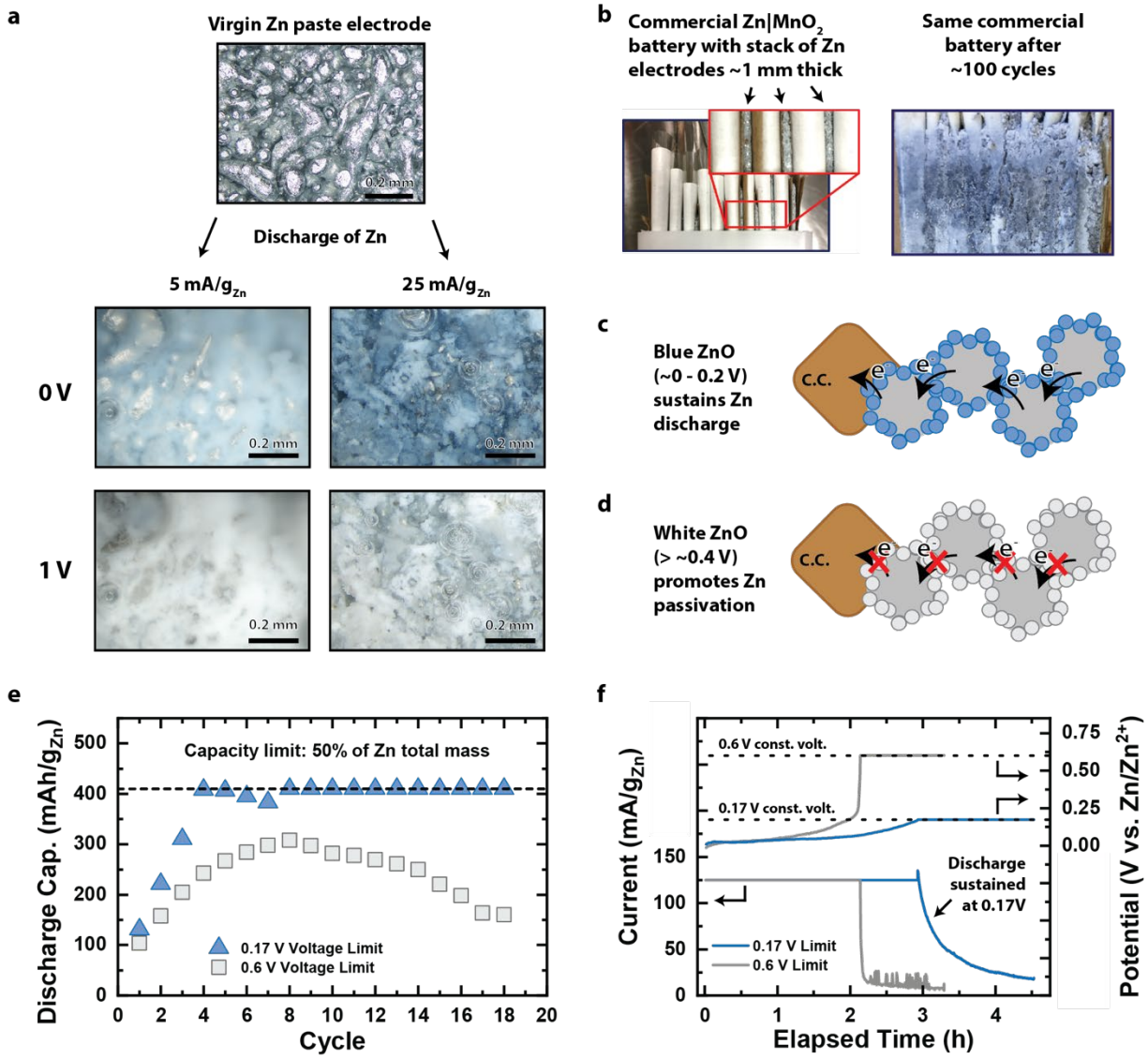


**Figure 1.** (a) Microscopy of industrial-design Zn paste electrodes after 5 mA/g or 25 mA/g discharge to 50% of theoretical capacity: (top) before discharge, (middle row) discharged and held near 0.0 V, (bottom row) discharged and held near 1.0 V. (b) ZnO formed in a 30 Ah commercial battery after typical cycling. (c) A schematic of electron transport in a Zn anode with conductive ZnO, and (d) with non-conductive ZnO. (e,f) Cycling performance of two Zn anodes, one controlled to always hold electroactive ZnO in its conductive state (cell A), the other uncontrolled allowing electroactive ZnO to become non-conductive (cell B).

The electroactive form of ZnO is likely to be widespread in commercial Zn alkaline batteries, as exemplified by the factory-made (Urban Electric Power Inc) 30 Ah Zn-manganese dioxide ($MnO_2$) alkaline battery shown in Figure 1b before and after ~100 cycles, where the blue ZnO growth covers all electrodes during cycling. Typical industrial-design paste-zinc electrodes consist of

packed particles (Figure 1a). The material properties of ZnO formed in these paste-zinc electrodes are important because electrical current must travel from particle to particle through this ZnO material to arrive at the current collector (Figure 1c and 1d), thus it is imperative the ZnO conductivity be high enough to carry electrical current. Figure 1e shows the benefit to performance of two industrial-design Zn anodes attempting 50% cycling of the Zn theoretical capacity, very high for typical operation, wherein cell A keeps the ZnO always in the conductive state (blue triangles) and cell B allows the ZnO state to change freely in an uncontrolled manner (grey squares). All known industry or literature cells operate like cell B. Conductive-state ZnO achieves the target 50% Zn utilization and maintains cycling much better than cell B (experimental details available in Materials and Methods). Figure 1f shows the resulting current and anode overvoltage of these two cells during a discharge procedure, where the overvoltage was used as the control variable to keep the ZnO in the blue-conductive state. The sharp drop of current seen in the grey curves of Figure 1f is classic passivation, whereas the tapered current seen in the blue curves is not.

The remarkable performance improvement of Figure 1e arises from control of the ZnO electronic properties and warrants a controlled and focused study on the ZnO itself. Repeatable and controlled formation of electroactive ZnO can be accomplished in aqueous KOH electrolyte by maintaining 20 mA/cm$^2$ discharge at the cut edge of Zn foil embedded in a pore channel (**Figure 2**a and Video S1), or by holding the cut Zn foil at 0.2 V for ~1 hr (Figure S5). This same procedure in aqueous NaOH or CsOH solutions also produces electroactive ZnO (Figure S24), but aqueous LiOH produces only the inert classical ZnO (Figure S23), which is explained in section 2.5. Discharge of Zn proceeds via the following reaction in which surface layers of zinc dissolve

(2) $Zn + 4OH^- \leftrightarrow 2e^- + Zn(OH)_4^{2-}$

and can then form a layer of ZnO (Figure 2a(iii)) by precipitation of zincate $Zn(OH)_4^{2-}$ ions

(3) $Zn(OH)_4^{2-} \leftrightarrow ZnO + H_2O + 2OH^-$

or possibly by direct solid-state discharge of the Zn metal.[11,12]

(4) $Zn + 2OH^- \leftrightarrow 2e^- + ZnO + H_2O$

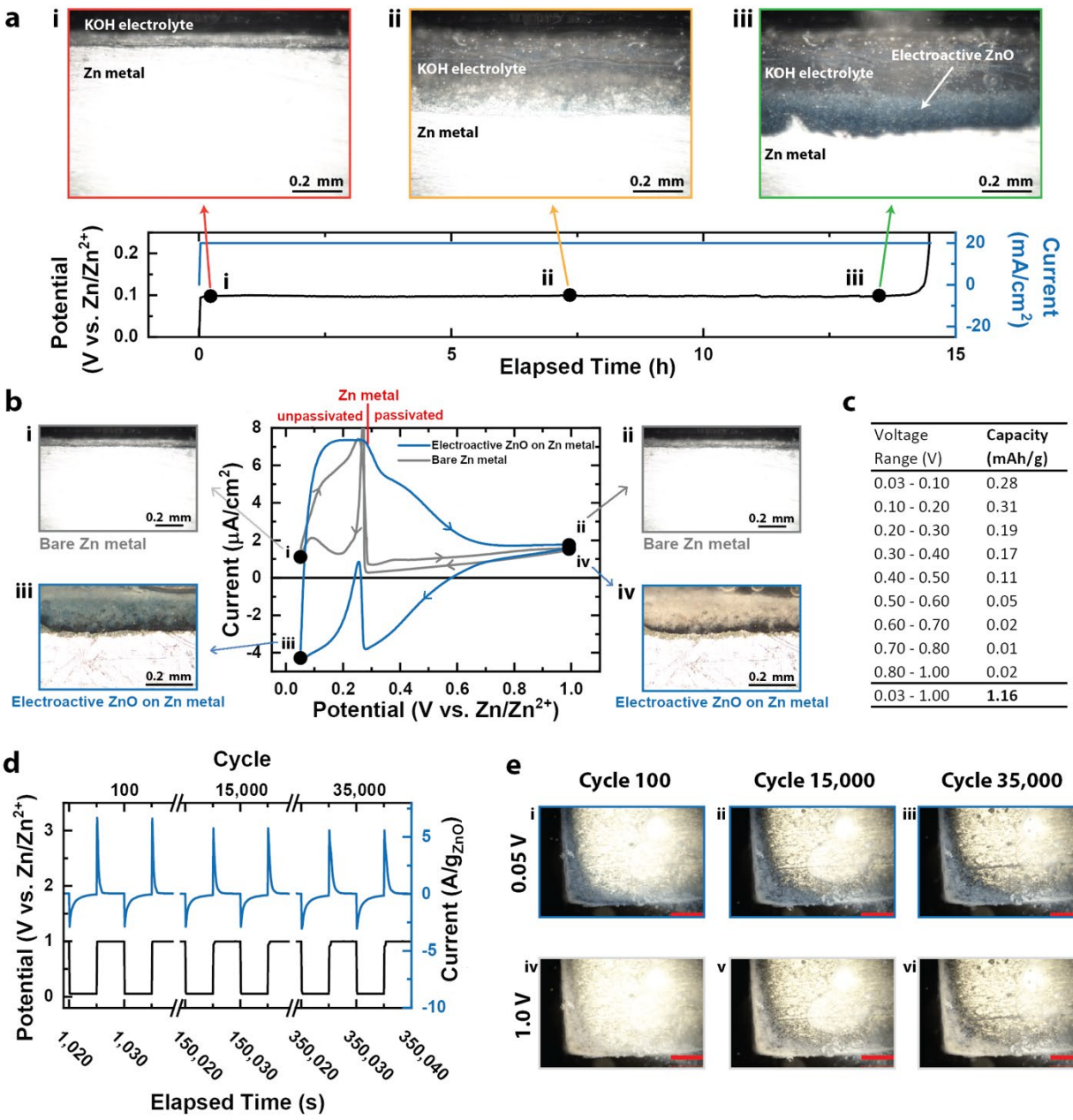


**Figure 2.** Electrochemical characterization and operando optical microscopy of Zn foil electrode in KOH electrolyte. (a) Optical microscopy during galvanostatic discharge (20 mA/cm$^2$) of Zn foil. (b) Cyclic voltammetry (1 mV/s) on bare Zn foil and on ZnO on Zn foil with visible light photographs for bare Zn foil (i, ii) and ZnO on Zn foil (iii, iv) at 0.05 V and 1 V, respectively. (c) Electroactive ZnO capacity measurements. (d) Cyclability assessment: chronopotentiometry of electroactive ZnO on Zn foil for selected cycles 100, 15,000, and 35,000. (e) Optical microscopy of ZnO on Zn foil at (i) 0.05 V, cycle 100, (ii) 0.05 V, cycle 15,000, (iii) 0.05 V, cycle 35,000, (iv) 1.0 V, cycle 100, (v) 1.0 V, cycle 15,000, and (vi) 1.0 V, cycle 35,000. Scale bar: 0.5 mm.

Growth of the ZnO layer does not begin simultaneously with Zn discharge, but shows a delay, likely because the electrolyte needs to become supersaturated with zincate before ZnO deposition proceeds, suggesting reaction (3) dominates over (4). After the blue-state electroactive ZnO layer grows very thick (300 to 500 μm), it shows "passive" behavior, meaning negligable current in response to steady overvoltage (Figure S4) [27,28], and yet if the voltage is rapidly switched between ~0.05 V and >0.6 V it changes color between blue and white (Figure 2b) with simultaneous passage of current (appx. 1 $e^-$ per 300 ZnO units, 1.36 x $10^{20}$ $e^-$ per $cm^3$ of ZnO, 1 mAh per $g_{ZnO}$) that is quantified in Figure 2c (raw data in S.I. Section 4). This electrochemical color change, which is classic electrochromism,[6,29] is highly reversible, and over 30,000 cycles are easily demonstrated (Figure 2d and 2e and Video S2 and S5). This system produces only one other type of material, which is a thinner layer of "amber" wurtzite ZnO created after the electroactive ZnO layer is held at >0.2 V for several hours (Video S3), discussed further in Section 2.5.

**2.2 Conductivity variations of electroactive ZnO in alkaline environments**

We directly measured the electroactive ZnO conductivity with operando electrical impedance spectroscopy measurements (**Figure 3**a, S.I. Section 9). As discussed in the introduction, classical ZnO has a single-crystal resistivity near $10^2$ Ω-cm[21] and conduction band electron concentration $n_e$ near $10^{15}$ $cm^{-3}$. In powder samples, classical ZnO resistivity can exceed $10^8$ Ω-cm. [22] However, here we show electroactive ZnO resistivity is subject to large but controllable variations as a function of potential. We performed operando impedance spectroscopy measurements on the electroactive ZnO while it was held at various voltages (Figure 3a, S.I. Section 9). The electroactive ZnO voltage is controllable because it is connected to the zinc foil electrode. When this electroactive ZnO material is held at ~0.02 V, its resistivity is ~1 Ω-cm, but when it is held at higher voltage, its resistivity increases by factors up to $10^4$ (Figure 3b).

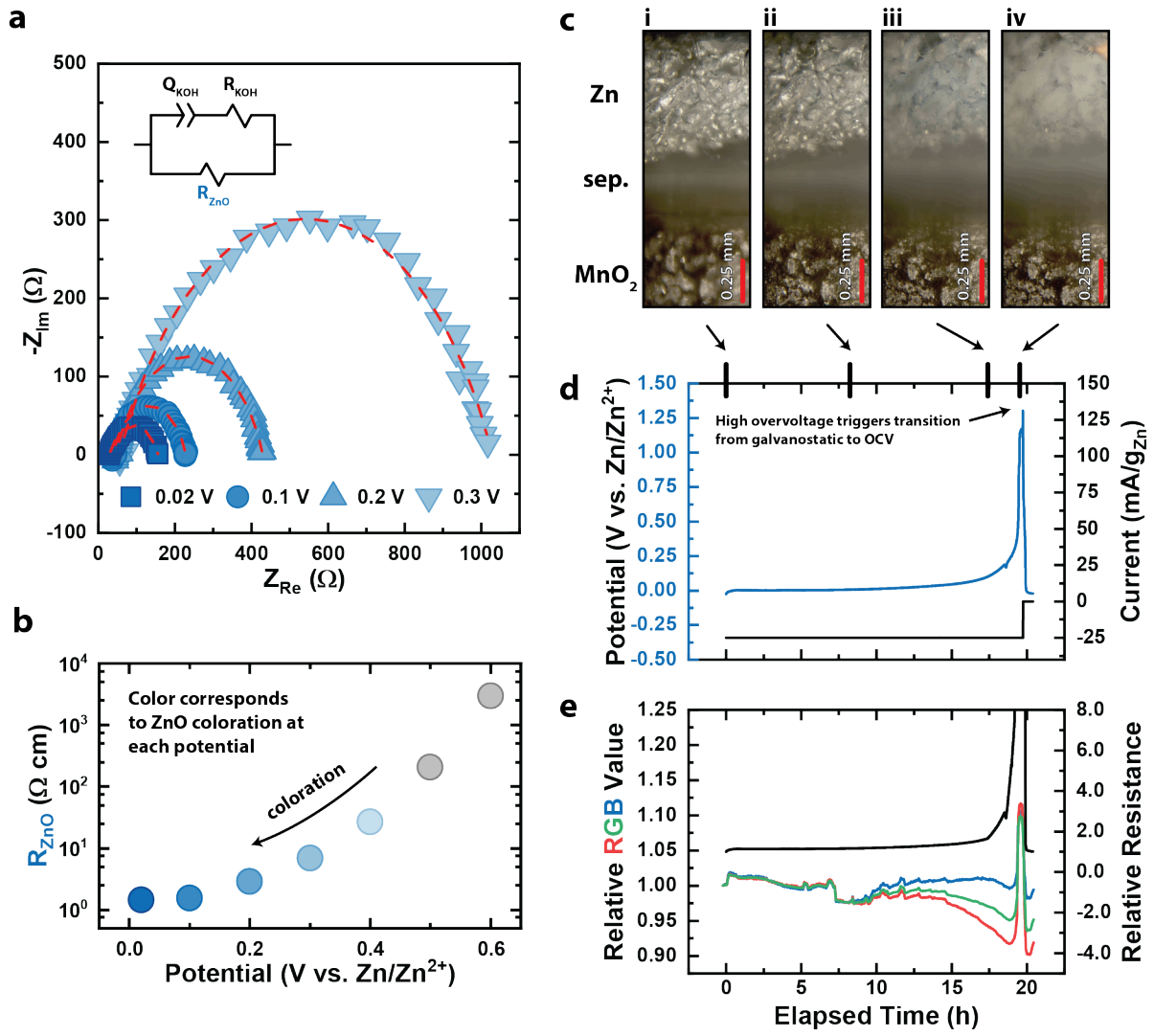


**Figure 3.** Operando impedance spectroscopy and galvanostatic discharge of a Zn-alkaline battery with operando optical microscopy. (a) Complex plane plot of impedance data (150 kHz to 1 Hz) with model fits in red dashed lines (inset: model), (b) ZnO resistivity from model vs electrode potential, (c) visible light photographs taken in operando of Zn, cellophane separator (sep.), and $MnO_2$, scale bar 0.25 mm, at (i) start of discharge, (ii) just before formation of ZnO, (iii) after formation of blue ZnO, and (iv) during passivation of Zn electrode, (d) Zn paste electrode potential vs. Zn reference with associated current to $MnO_2$, and (e) relative RGB color values (red, green, and blue curves) from in operando imaging of Zn electrode and relative ZnO resistivity (black curve) vs. Zn equilibrium, estimated by linear interpolation of impedance data.

The resistivity of electroactive ZnO is clearly of great importance to the performance of rechargeable Zn battery electrodes via its role in passivation. To demonstrate the importance of electroactive ZnO for passivation, we repeated the 25 mA/g discharge experiment of Figure 1a but allowed it to continue past 50% of theoretical capacity, until the electrode passivated (Video S4

and Figure 3c), with simultaneous measurement of overpotential and current (Figure 3d). A video of this passivation process shows the electroactive ZnO to physically encapsulate (Figure 3c(iii)) the Zn metal particles in core-shell geometries. Passivation is evident in these data when the overvoltage rapidly rises higher in response to increased resistance to passage of current (Figure 3d). Simultaneous to this rapid rise in voltage, the color of the ZnO changes from blue to white (Figure 3e and 3c(iv)) for reasons discussed in section 2.3. The correlation between voltage and ZnO resistivity is reliable and repeatable (Figure 3b), thus we use the electrode voltage as a proxy measurement of the ZnO resistivity during this 25 mA/g discharge process (Figure 3e).

An order-of-magnitude model provides rough verification that ZnO ohmic resistivity causes electrode passivation. The Zn-paste electrode is ~800 μm thick and is comprised initially of ~50 μm Zn particles. At the time of passivation, the Zn particles had discharged 60% of their theoretical capacity and thus were covered with a layer of ZnO. The current density was forced along a pathway through these layers as drawn in Figure 1d. Based on the 60% discharge, the layers of electroactive ZnO between the Zn particles were ~20 μm thick at the time of passivation. Thus, to maintain discharge, electrical current (~5 mA/cm$^2$ superficially) is estimated to travel through ~300 μm worth of "in-series" ZnO layers to arrive at the current collector, as drawn in the schematic of Figure 1d. Ohm's Law can thus be used to estimate a <1 mV drop along this path for blue-state electroactive ZnO and a ~500 mV drop for white-state electroactive ZnO. Overvoltages above ~200 mV lead toward passivation, suggesting a clear first-principles physical mechanism for passivation of Zn in alkaline batteries by electroactive ZnO. This blue-white change of color finally explains the "type I and type II" ZnO discussed in passivation literature.[3,12,30] Type I and II ZnO have been observed by their white and blue color, respectively, but neither have been explained or characterized in battery literature[31]. The very high conductivity of blue-state ZnO also explains the ability of single-discharge Zn alkaline batteries, for example a standard "D cell", to deep discharge from a ~15 mm thick cylindrical Zn-paste anode. Additional passivation may occur at the site of the electrochemical reaction due to reactant mass transfer limitations, but this seems to be of secondary importance after considering that the layers of electroactive ZnO exemplified in Figure 2a can grow up to 500 μm thick at 25 mA/cm$^2$ discharge before passivation is induced.

### 2.3 Optical absorption, band gap, and conduction band carrier concentration

To uncover the electronic mechanisms for the variable coloration and conductivity, operando UV-vis spectroscopy data were collected from electroactive ZnO grown as described in section 2.1 but in a UV-vis cuvette (**Figure 4**, Video S5). A specular reflection geometry was used (Figure 4b), with wavelengths from 300 to 850 nm, to collect a full UV-vis absorption spectrum at eleven voltages ranging from 0.01 to 1.0 V. Because the ZnO layer is a bonded powder (Figure S27 and S28), a Kubelka-Munk (*K-M*) diffuse reflectance analysis[32] was performed to quantify the ZnO optical absorption coefficient $\alpha$ as a function of potential (details and *K-M* calculations of $\alpha$ are given in S.I., Section 6). The absorption coefficient data $\alpha$ are then analyzed with a Tauc plot to calculate the ZnO band gap $E_g$ as a function of potential. The changes to $E_g$ are then used to calculate conduction band electron concentration, $n_e$, via the Burstein-Moss model in which inserted electrons raise the Fermi level in the conduction band and increase the energy required to promote an electron from the valence band to free states.

Classical ZnO has a small visible absorption coefficient, $\alpha$, near 1 $cm^{-1}$ but high reflectance near 10% in the visible range,[20] resulting in its white color. In contrast, we measure the visible absorption coefficient of "blue-state" electroactive ZnO to be higher than classical ZnO by a factor of $10^2$ in blue wavelengths and by $10^4$ in red wavelengths (Figure 4c). This disparity in absorption between red and blue wavelengths causes the blue coloration of the material. When it is held at voltages >0.6 V its absorption coefficient is more equal to that of classical ZnO, rendering its coloration white. This change of optical absorption is due to the increase of conduction band electrons caused by the electrochemical reaction measured in Figure 2b and 2c, further analyzed in Figure 4g as discussed below.

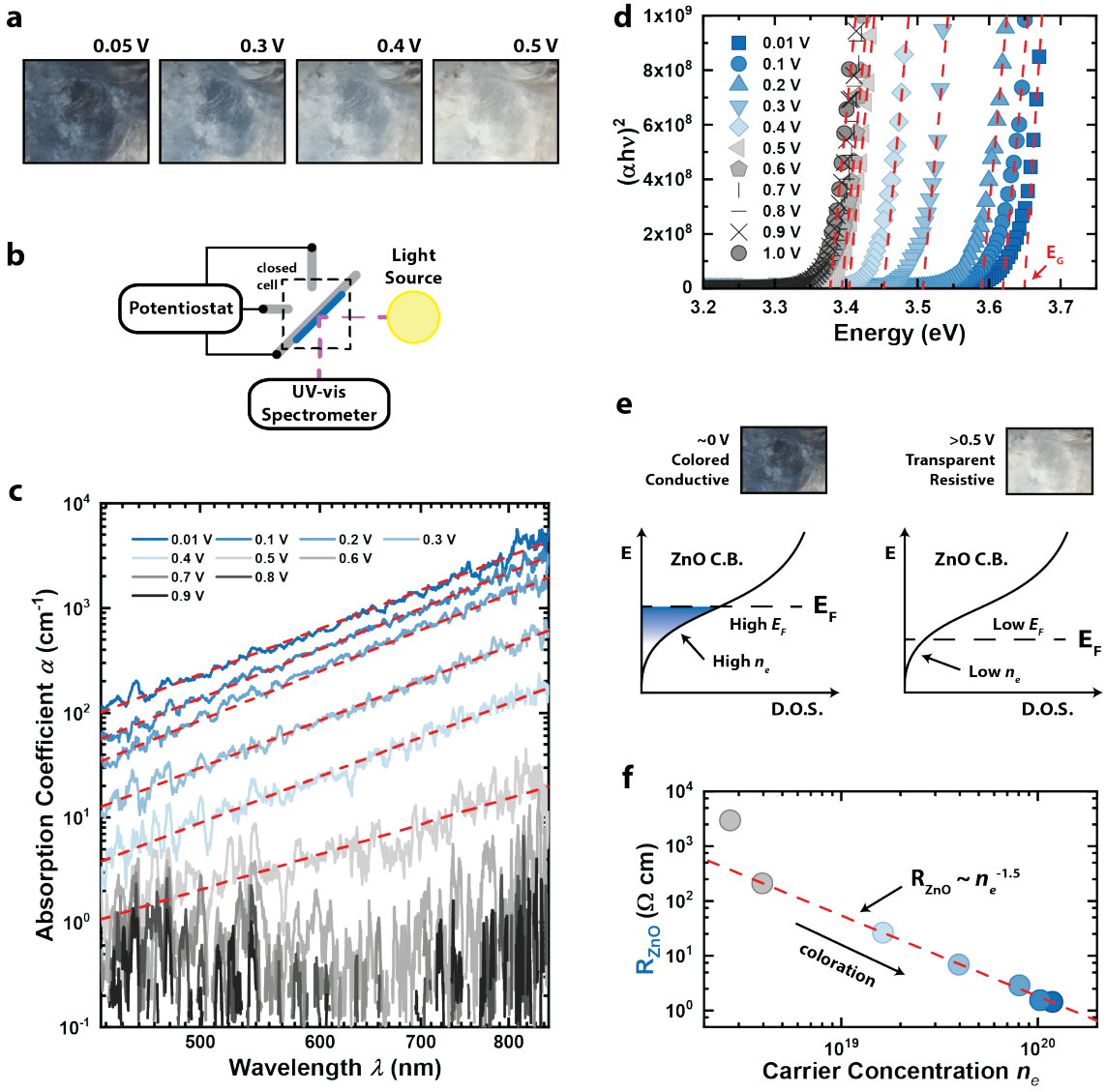


g

| Potential (V) | 0.01 | 0.05 | 0.1 | 0.2 | 0.3 | 0.4 | 0.5 | 0.6 | 0.7 | 0.8 | 0.9 | 1.0 |
|---|---|---|---|---|---|---|---|---|---|---|---|---|
| $n_e$ Burstein-Moss ($cm^{-3}$ x $10^{20}$) | 1.250 | 1.138 | 1.031 | 0.806 | 0.396 | 0.163 | 0.040 | 0.027 | 0.013 | 0.013 | 0.007 | 0.004 |
| $n_e$ Coulometry ($cm^{-3}$ x $10^{20}$) | -- | 1.360 | 1.024 | 0.661 | 0.443 | 0.246 | 0.115 | 0.057 | 0.039 | 0.029 | -- | -- |
| Band Gap $E_G$ (eV) | 3.65 | 3.64 | 3.62 | 3.59 | 3.51 | 3.54 | 3.4 | 3.39 | 3.39 | 3.38 | 3.38 | 3.38 |
| Power Law Exponent $\alpha \sim \lambda^b$ | 5.52 | 5.75 | 5.89 | 5.92 | 5.69 | 5.61 | 4.29 | -- | -- | -- | -- | -- |

**Figure 4. Operando UV-vis spectroscopy.** (a) Visible light photographs of ZnO at different potentials; (b) schematic of UV-vis setup; (c) electroactive ZnO absorption coefficient vs. absorbed light wavelength at different potentials with power law fits, red dashed lines; (d) Tauc plot for band gap calculation; (e) schematic of increased carrier concentration and absorption at low potential; (f) ZnO resistivity vs. carrier concentration with power law fit in red dashed line; (g) table of calculations (row 1) carrier concentration calculated via Burstein-Moss effect, (row 2) carrier concentration

calculated from electrochemical data in Figure 2c, (row 3) band gap calculated from data in (d), and (row 4) power law exponents from (c). Running average over 15 points (5 nm) used to reduce noise for Figure 4c and Figure 4d.

The Tauc plot analysis of the absorption data reveals changes in the bandgap of electroactive ZnO as a function of potential (Figure 4d), and ultimately allows calculation of conduction band electron concentration $n_e$. When electroactive ZnO is held near 1.0 V, we measure a band gap of ~3.38 eV (Figure 4d), close to the literature consensus of 3.37 eV. [7] Decreasing its potential to 0.02 V results in a band gap increase to 3.65 eV. Assuming this shift of bandgap is due to raising of the Fermi level (Figure 4e) due to the Burstein-Moss effect,[33] consistent with prior work,[9] $n_e$ can be calculated [34] as

(1) $\Delta E_G = \frac{h^2}{8\pi}\frac{(3\pi^2 n_e)^{3/2}}{m^*}$

Non-parabolicity of the band gap is accounted for with $m^*$ [35] according to

(2) $m^* = m_0^*[1 + 2a(\Delta E_G)]$

where $\Delta E_G$, $h$, $n_e$, $m_0^*$, and $a$ are the band gap shift, Planck's constant, ZnO effective electron mass, and non-parabolicity parameter, respectively. The parameter, $a$, was taken as 0.29 $eV^{-1}$, per the literature. [36] The resulting values of are in good agreement with the electrochemical measurements of coulombs passed through the electrode during this process (Figure 4g). Combining these data with those from section 2.2, a connection emerges between resistivity $R_{ZnO}$ and conduction band electron concentration $R_{ZnO} \sim n_e^{-1.5}$ (Figure 4f). Although the $n_e^{-1.5}$ trend deviates from theoretical predictions of $R_{ZnO} \sim n_e^{-1}$ for ionized-impurity scattering,[39,37] it agrees with empirical measurements from magnetron sputtered ZnO under zinc-rich conditions. [38]

For the electroactive ZnO in its blue state, a power law correlation exists between the optical absorption coefficient $\alpha$ and wavelength $\lambda$, $\alpha \sim \lambda^b$ (Figure 3c). This power law dependence is consistent with a free carrier absorption mechanism for coloration[39,40,41] facilitated by either a phonon-assisted or a charged-impurity-assisted mechanism. Theory[39,40] predicts $b = 3$ for phonon-assisted absorption and $b = 5$ for charged-impurity-assisted absorption. Our measured value of $b \approx 5.75$ (Figure 3g, S8, S9) when the ZnO is visibly blue (0.4 V and below) is close to the theoretically predicted one for charged-impurity-assisted free carrier absorption.

Another correlation exists between the optical absorption coefficient and conduction band concentration, $\alpha \sim n_e^c$, where $c$ is approximately 1.6 and increases with wavelength (Figure S8 and S9). Theory predicts $c \sim 2$ for charged-impurity-assisted absorption and $c \sim 1$ for phonon-assisted absorption. [39,42] The $n_e^{1.6}$ trend here causes stronger dependence of absorption on $n_e$ than most

electrochromic materials, such as $WO_3$, which are often suggested to color by phonon-assisted free-carrier absorption. [43] Though our results are consistent with charged-impurity-assisted free carrier absorption, and we know charged-impurities intercalate during the electrochemical reaction, prior work on nanocrystal dispersions of electroactive ZnO showed evidence that plasmonic resonance was responsible for optical absorption. [44] Thus, the mechanism for light absorption requires further study for full clarification.

**2.4 Applications, innovations, and devices based on electroactive ZnO**

Reviews of ZnO electrochemistry or electrode design[2,25,27] contain, at present date, no mention of the huge variation of ZnO conductivity revealed in this report. Knowledge of this phenomenology provides an opportunity for improved battery design because (i) it explains why zinc alkaline electrode failure is, at least in many cases, due to the conductivity changes of electroactive ZnO and (ii) it allows for design of control tactics to reliably keep ZnO conductivity higher. Figure 1e shows the advance in performance possible for a Zn alkaline anode cycled at 50% of its theoretical capacity due to control of the ZnO conductivity via electrode overvoltage. Further, because electroactive ZnO hosts rapid intercalation capacity (10 F/g or 50 F/cm$^3$ ignoring double-layer contributions) with high-cyclability, it can serve a secondary purpose as an electrochemical capacitor near its operating voltage ~0.01 V to ~0.3 V. Since this ZnO capacity can be accessed simultaneously with the Zn metal conversion reaction, there exist possibilities for a hybrid conversion-intercalation (battery-supercapacitor) device that can deliver high power capacity on short time scales and high energy density on long time scales. Although intercalation capacity of this ZnO is lower than stand-alone supercapacitors,[45] which can host ~100 F/g or ~100 F/cm$^3$, ZnO delivers its benefits without added costs.

Though we focus mainly on battery applications in this report, electroactive ZnO is also a candidate for electrochromic applications. The infrared absorption shown in Figure 4 results in remarkable coloration efficiencies (*CE*) as calculated by $CE = (\alpha\, t)/(Q/A)$ where $t$, $Q$, and $A$ are film thickness, charge transferred, and electrode area, respectively (S.I. Section 7). Coloration efficiency is 50 cm$^2$/C at 450 nm, 1,000 cm$^2$/C at 700 nm, and is expected to increase well above 1,000 cm$^2$/C in the infrared. Typical coloration efficiencies for other high-efficiency electrochromic materials, including $WO_3$,[29] are on the order of 100 cm$^2$/C, making electroactive

ZnO a high-efficiency electrochromic material ideally suited for red or infrared absorption in electrochromic windows and switchable heat shields.

Finally, our impedance measurements in Figure 3 show a factor $10^4$ change in resistivity, easily controllable by an external voltage. Since this change in resistivity is highly reversible, wherein we showed facile 35,000 cycles without degradation, there may be possible applications in resistance-based memory[46] or novel approaches to specialty transistors. [47,48]

### 2.5 ZnO Crystal Structure and Reaction Stoichiometry

Existing studies led by Mayer and Gamelin rigorously characterize the electrochemical reactions in nanocrystalline ZnO, including dependence on volume and intercalating cation. [9,10,49,50,51,52] However, these studies focused mainly on nanocrystalline (<10 nm) dispersions and did not identify or discuss the crystal structure or defects that enable or participate in the electroactivity and that differentiate it from classical ZnO. These defects are present at ~$10^{20}$ $cm^{-3}$ (1 defect per ~300 ZnO units) based on the coulometry and carrier concentration measurements of Figures 2 and 4. In this section we present advanced characterization towards better understanding of these crystal defects and other details of the ZnO electrochemical intercalation reaction.

Operando synchrotron X-ray diffraction (XRD) of electroactive ZnO during the blue-white electrochemical transitions (**Figure 5**a, 5b) show that wurtzite crystal structure is the only crystal phase present during this reaction, to within the XRD detection limit (0.4% of the wurtzite peaks). The XRD data also show a contraction of the *d*-spacing as electrode potential changes from 0.02 V to 0.6 V but negligible contraction for potentials above 0.6 V (Figure 5c, S20, and S21), which correlates well with the removal of electrons and cations (see $n_e$ in Figure 4g). This lattice contraction can be explained by the reduced electric-field screening between $Zn^{2+}$ and $O^{2-}$ ions when conduction band electron concentration decreases. As expected, voltage changes above 0.6 V cause minimal changes to $n_e$.

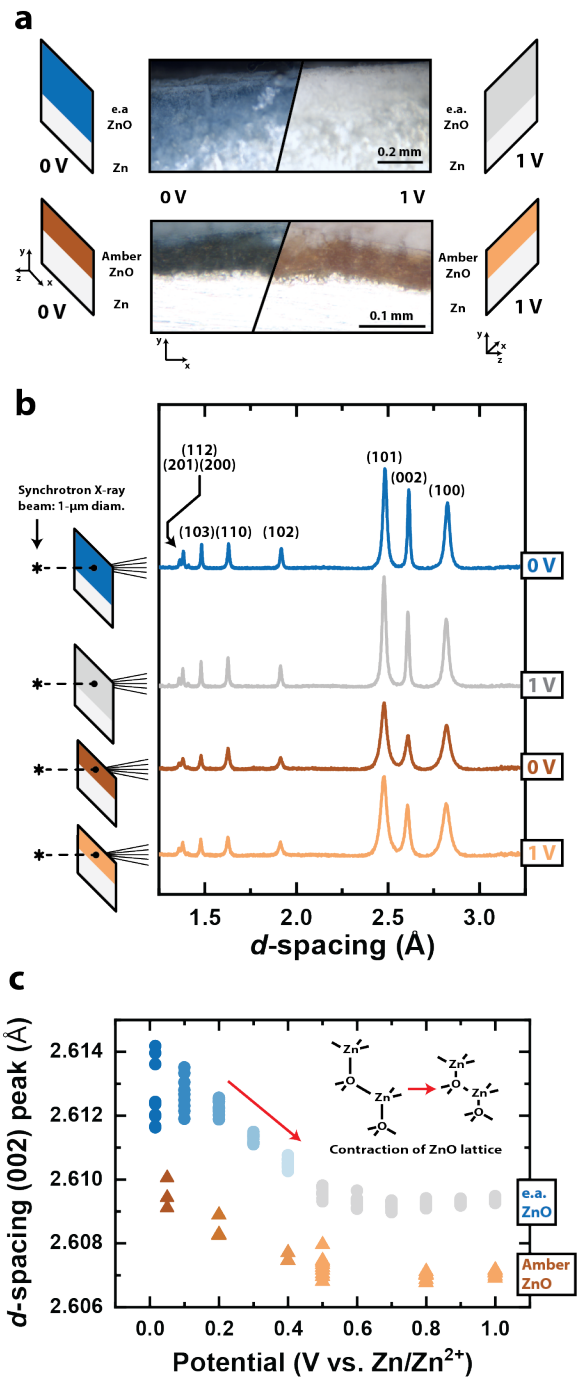


**Figure 5.** Operando synchrotron XRD. (a) Schematic and visible light photographs of electroactive and amber ZnO on Zn foil, (b) synchrotron XRD patterns with ZnO reflections indicated, (c) d-spacing of (002) ZnO reflection as a function of electrode potential (inset: schematic of ZnO lattice contraction).

As mentioned in Section 2.1, when the potential of Zn metal covered in electroactive ZnO is held >0.2 V for several hours, the Zn forms an additional layer of amber-tinted ZnO (Video S3).

This "amber ZnO" also undergoes electrochromic color change (Figure 5a) but retains some of its amber color throughout. The operando XRD measurements show this amber ZnO is also wurtzite ZnO (Figure 5b), but its wurtzite reflections are broadened, likely due to increased disorder. Amber ZnO is reported in the literature via several different synthesis methods,[53,54,55] and its color is attributed to oxygen vacancy defects, discussed later in this section.

To investigate the molecular-scale nature of the defects that enable ZnO electroactivity, we performed quantitative solid-state $^{1}$H MAS NMR spectroscopy to compare and quantify proton defect environments (**Figure 6**) in the blue vs white states. The accuracy of this comparison was maximized by performing the NMR first on a blue-state ZnO sample then oxidizing that sample to the white state in the NMR rotor by removing the cap and exposing it to air for 2 h. This kept the ZnO mass constant. NMR measurements were then repeated on the resulting white-state sample. The solid-state $^{1}$H NMR spectra reveal that the electroactive ZnO samples show multiple $^{1}$H peaks associated with defect and surface environments. The resolved $^{1}$H peaks span from approximately 0.5 to 2.5 ppm, with also an intense $^{1}$H signal at 4.9 ppm due to liquid $H_2O$ in the aqueous electrolyte. The solid-state $^{1}$H MAS NMR spectra for the blue vs. white states are nearly identical except for the blue-state having higher intensity at the 0.9, 1.3, 1.6, and 2.0 ppm peaks (Figure 6a, 6b). Since the NMR is quantitative, these differences in integrated signal intensity suggest these peaks to be associated with intercalating protons active in the electrochemical reaction that cause blue-white color change. Quantitative analysis of the difference spectrum indicates that the ZnO in the blue state ZnO holds 0.7 x $10^{20}$ $cm^{-3}$ more inserted protons associated with these four $^{1}$H signals than the white state ZnO (S.I., section 11). This quantity is in good agreement with the electrochemical and UV-vis measurements (~1.0 x $10^{20}$ $cm^{-3}$), within experimental error, further supporting the conclusion that protons electrochemically intercalate during the coloration process.

Existing literature is conflicted on the precise identity of these $^{1}$H NMR signals. Using $^{1}$H-$^{17}$O TRAPDOR NMR experiments on $^{17}$O-enriched ZnO, Wang et al.[56] indicate that $^{1}$H signals between 0 and 2 ppm are associated with protons occupying oxygen vacancies ($H_O$). However, Li et al.[57] used 2D dipolar-mediated $^{1}$H{$^{1}$H} triple-quantum single-quantum correlation experiments to measure that the $^{1}$H signal at 1.3 ppm is associated with groups of three protons in sub-nanometers scale proximity, which they suggest are -ZnOH "nests" within zinc vacancies ($H_{Zn}$). Wang et al. [58] suggest that these signals are due to surface hydroxyl protons and chemisorbed

water, as they are removed upon heating and reappear following water re-adsorption in air. Thus, the exact identity of these species cannot be assigned from a literature review alone. To determine the precise position of protons in the ZnO lattice, we propose future NMR studies using $^{67}$Zn enriched ZnO or neutron scattering experiments.

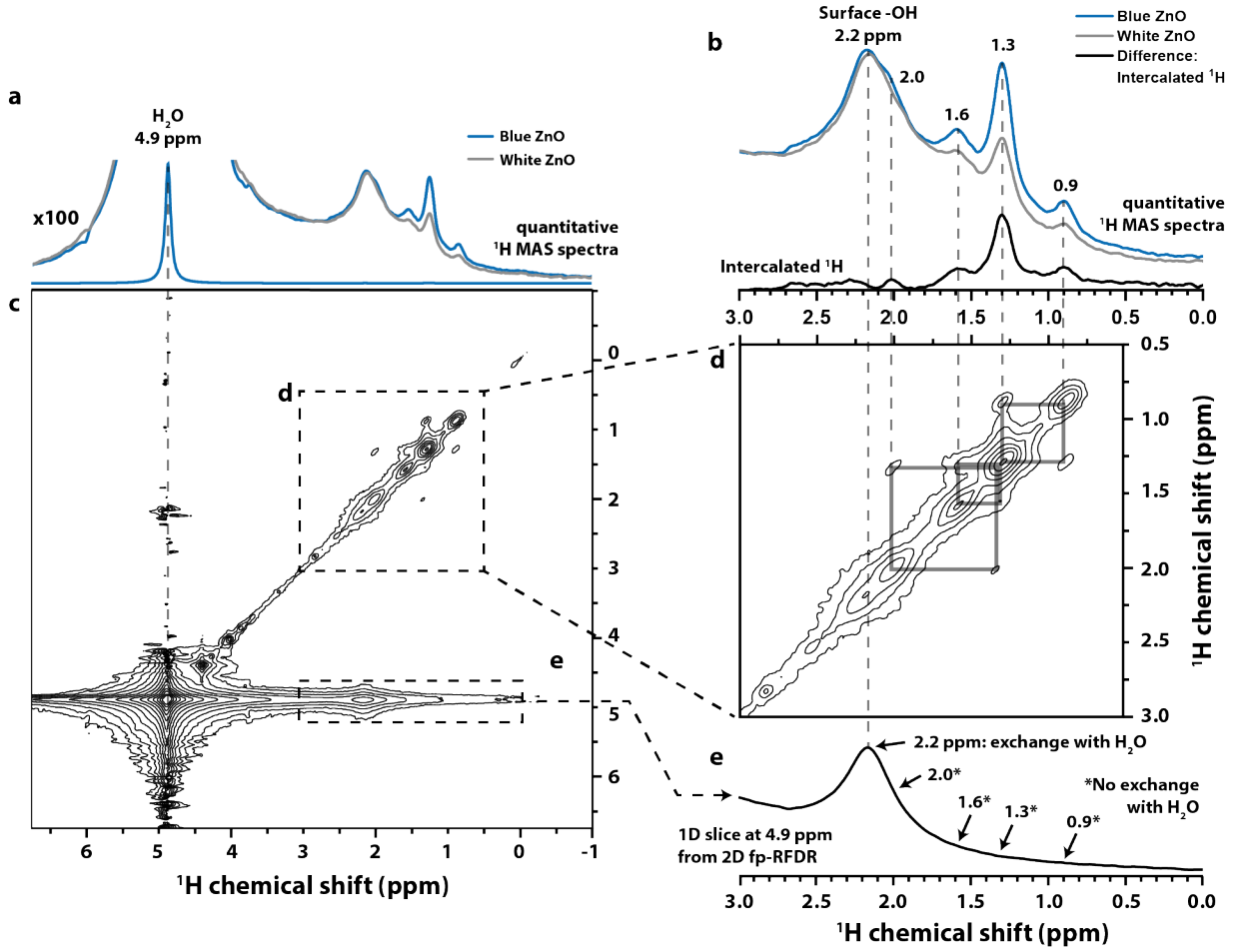


**Figure 6**: Multi-dimensional solid-state $^{1}$H NMR spectra acquired on electroactive ZnO at 10 kHz MAS and 14.1 T. (a) Quantitative $^{1}$H MAS NMR spectra of electroactive ZnO in the blue and white states, including (b) the region containing the defect and surface environments of interest. The quantitative difference spectrum (black) between blue and white electroactive ZnO establishes multiple unique environments associated with intercalated protons. (c) 2D $\{^{1}H\}^{1}H$ fp-RFDR NMR spectrum acquired on blue electroactive ZnO with a mixing time of 9.6 ms. Note that $T_1$ noise associated with the intense $H_2O$ signal obscures the correlated 2D signal intensity in the indirect dimension between $H_2O$ protons at 4.9 ppm and ZnOH surface protons at 2.2 ppm. (d) 2D region of interest illustrating that the intercalated protons are dipole-dipole coupled and thus in close sub-nanometer-scale proximity to each other (solid grey lines). (e) Selected 1D slice from the 2D $\{^{1}H\}^{1}H$ fp-RFDR spectrum that illustrates the proton environments centered at 2.2 ppm are exchanging with $H_2O$ and are therefore surface species.

To gain further insight into the nature of these $^{1}H$ environments, we acquired a solid-state 2D $^{1}H\{^{1}H\}$ finite-pulse radio frequency driven recoupling (fp-RFDR) spectrum (Figure 6c, 6d) on the electroactive ZnO in the blue state, which recouples $^{1}H$ nuclear spins via through-space (<1 nm) dipole-dipole interactions. Therefore, off-diagonal peaks in the 2D spectrum are created by $^{1}H$ nuclei that are either (i) immobile but sufficiently proximate in space (<1 nm) to couple via dipole-dipole interactions, or (ii) mobile enough to exchange between sites at a rate faster than the experimental mixing time. [59] The 2D $^{1}H\{^{1}H\}$ fp-RFDR NMR spectrum reveals an off-diagonal peak created by the liquid $H_2O$ at 4.9 ppm and the $^{1}H$ peak at 2.2 ppm (Figure 6e). The liquid $H_2O$ dipole-dipole interactions average to zero due to rapid orientation fluctuations. Thus, the 4.9 to 2.2 ppm off-diagonal peak must be due to proton exchange between liquid $H_2O$ and a ZnO surface site, perhaps an adsorbed hydroxyl species. Other off-diagonal peaks exist between the 1.3 ppm signal and the 0.9, 1.6, and 2.0 ppm signals (Figure 6d), none of which exchange with liquid $H_2O$ in the electrolyte (Figure 6e), suggesting they are bulk-crystal proton defect sites. As already mentioned with Figure 6b, these same sites are more populated in the blue state vs. the white state, indicating protons insert into these environments during the blue coloration transition.

It is curious that the proton environments at 0.9, 1.3, 1.6, and 2.0 ppm persist even after the ZnO changes to the white state (Figure 6b, gray spectrum). This may be due to different defect environments that produce $^{1}H$ MAS NMR signals at the same ppm shift, or alternatively the protons may play a more complex role than one-for-one insertion with the conduction band electrons, and hydrogen doping in general may affect ZnO properties.

To determine if other cations, beside $H^+$, can intercalate as the charge-balancing cation, we placed our dry electroactive ZnO into a THF:toluene mixture in an argon glove-box then added chemical reductant along with a single salt (either $LiBF_4$, NaTFSI, KTFSI, or CsCl) as described in previous literature[52] and outlined in the Materials and Methods section. These experiments prove that $Li^+$, $Na^+$, $K^+$, or $Cs^+$ in addition to $H^+$ can intercalate into electroactive ZnO to charge-balance inserted electrons. Classical ZnO cannot undergo these reactions with the same techniques (Figure S23a), indicating crystal defects present in electroactive ZnO must play a key role. Supporting this hypothesis is that ZnO formed rapidly is more electroactive than ZnO formed slowly (Figure 1a). Among the crystal growth community, it is commonly accepted that faster crystal growth rate typically increases defects. Further supporting this hypothesis is that ZnO

grown in LiOH solution is not electroactive (Figure S23b), which agrees well with the fact that ZnO grows much slower in aqueous LiOH solutions than in KOH, NaOH or CsOH solutions.[60]

We sought to measure how much electrolyte cation was incorporated as a dopant during the same synthesis process of Figure 2. To address this, we repeated the synthesis of Figure 2 with NaOH or CsOH electrolyte, then used X-Ray fluorescence spectroscopy (XRF) to measure concentration of Cs and solid-state $^{23}$Na MAS NMR spectroscopy to measure concentration of Na in our electroactive ZnO samples (Figure S25), all of which show alkali concentrations lower than $0.4 \times 10^{20}$ cm$^{-3}$ in the ZnO solid, which is too low for them to be the defect, assuming a 1-to-1 stoichiometry with the electrochemical intercalation. A 2-to-1 or higher stoichiometry could be consistent, but alkali doping does not appear important considering electroactive ZnO is able to be synthesized without alkali cations.[9]

A more likely source of ZnO electroactivity is the formation of native Zn or O defects during crystal growth. To investigate this possibility, we performed operando confocal Raman spectroscopy on the electroactive ZnO (**Figure 7**). Raman spectra from the electroactive ZnO show vibrational signals characteristic of wurtzite ZnO including $E_2$ phonons and longitudinal optical (LO) phonons (Figure 7b). When the ZnO potential is held at 1.0 V (white state) the LO phonon peak at ~580 cm$^{-1}$ is stronger under 532 nm (2.33 eV) laser stimulation than under 633 nm (1.96 eV) stimulation. Conversely, when the ZnO potential is held near 0.0 V (blue state) that same LO peak is stronger under the 633 nm stimulation (Figure 7c). This ~580 cm$^{-1}$ LO phonon mode is absent in classical ZnO (Figure 7b). Amplification of the LO phonon mode is likely due to resonance Raman scattering,[61,62] indicating photon-coupled electronic transitions must exist deep within the bandgap and are affected by the ZnO blue-to-white transition. Indeed, the photoluminescence spectrum of the white electroactive ZnO shows a large quantity of photonic transitions deep within the band gap (Figure S26), whereas commercial pure ZnO does not. [63]

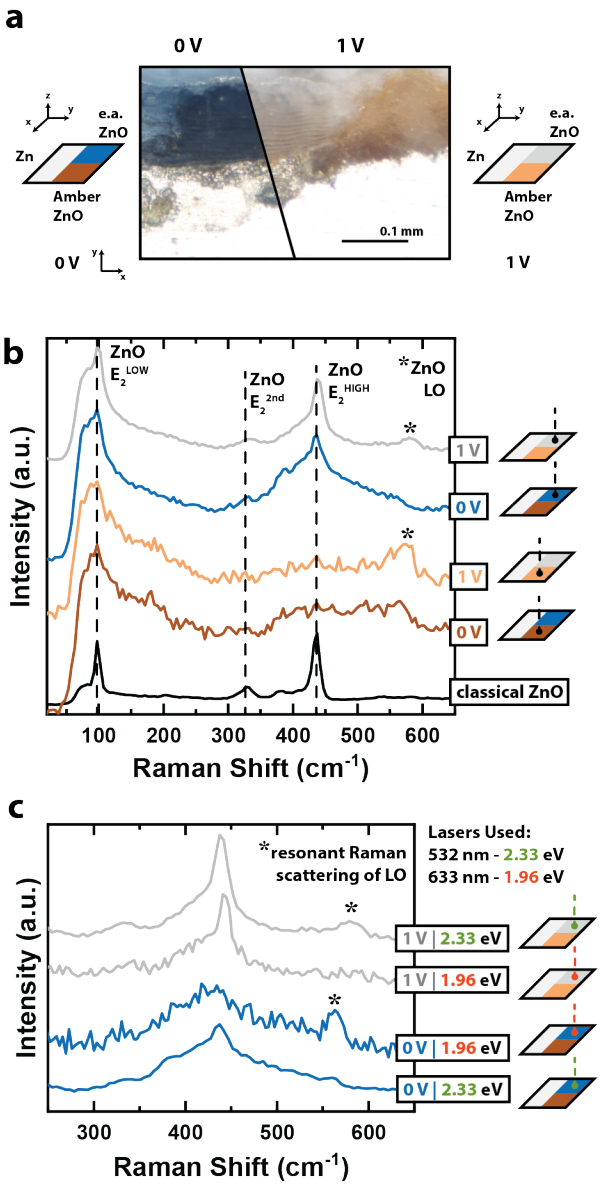


**Figure 7**: (a) Visible light photograph and schematic of electroactive and amber ZnO. (b) Operando confocal Raman spectroscopy on electroactive and amber ZnO at 0.0 V and 1.0 V and classical ZnO stimulated by 532 nm light. (c) Operando confocal Raman spectroscopy on electroactive ZnO at 0.0 V and 1.0 V stimulated by 532 nm and 633 nm light.

The amber ZnO provides clues regarding the native defect identity in electroactive ZnO. Although literature gives no explanation for blue-white electrochromism in ZnO, there are publications suggesting amber (red, orange) coloration of ZnO to be caused by oxygen vacancies, regardless of formation technique.[53,54,55] The Raman LO mode is stronger from the amber ZnO than from the blue or white electroactive ZnO (Figure 7b), and enhancement of the LO mode is

often hypothesized to indicate the presence of oxygen vacancies, $V_O$, in the ZnO.[64,65,66,67,68] Further, the $E_2^{high}$ Raman peak, which is associated with the oxygen sublattice, is significantly broadened in amber ZnO (Figure 7b), and our XRD data reveal smaller d-spacing and broader peak widths for amber ZnO than for electroactive ZnO (Figure 5b), which others claim is also correlated with increased oxygen deficiency[69,70] due to increased lattice disorder. Finally, amber ZnO grows on the Zn foil only once blue-white electroactive ZnO has first covered it (Video S3). This layer of blue-white ZnO may introduce mass transfer limitations that promote zinc-rich conditions near the Zn surface, which in turn would promote $V_O$ generation in ZnO formed near the zinc foil. Thus, we hypothesize $V_O$ defects host the cations that are electrochemically inserted during coloration, enabling ZnO electroactivity via formation of a $V_O$-cation complex. The vacancy $V_O$ alone is a deep donor in ZnO[7,71] and therefore is unlikely to contribute to conduction band electron concentration, but when a cation ($H^+$, $Li^+$, $Na^+$, $K^+$, $Cs^+$) occupies the oxygen-vacancy, a shallow electron donor could be formed. For example, $H^+$ complexing with an oxygen-vacancy forms a defect symbolized as "$H_O$" that is commonly believed to be a shallow donor in ZnO,[7,72] which donates an additional electron into the conduction band. This crystal structure reaction mechanism explains (i) the inactivity of classic ZnO vs. electroactive ZnO, and (ii) the increased conductivity and optical absorption in electroactive ZnO.

## 3. Conclusion

This report establishes that fast crystal growth rate of wurtzite ZnO in alkaline electrolytes creates a special wurtzite ZnO material called "electroactive ZnO", which reversibly inserts cations ($H^+$, $K^+$, $Na^+$, $Li^+$, or $Cs^+$) and conduction band electrons as a function of potential between 0.01 V to ~0.6V. We propose that crystal vacancy defects formed during rapid crystal growth complex with inserted cations to form shallow electron donors, ultimately increasing the conduction band electron concentration. Operando Raman spectroscopy indicates oxygen vacancies formed during crystal growth host the intercalated cations, and this feature distinguishes electroactive ZnO from classical ZnO, which has no electroactivity. Operando UV-vis and impedance spectroscopy confirm the conduction band electron concentration to determine the electrical conductivity, which is controllable to values spanning four orders of magnitude. Quantities of inserted electrons and cations were measured via solid-state $^1H$ MAS NMR spectroscopy to have a maximum concentration of ~1.4 x $10^{20}$ per $cm^3$. The advanced understanding reported here provides a first-

principles-based method to avoid Zn passivation as a failure mechanism in Zn alkaline battery anodes. Novel cycling protocol produces greatly improved performance at 50% utilization of the Zn theoretical capacity. This report also provides the first physics-based explanation of "type I and II ZnO" described in the Zn alkaline battery literature for many decades. The fast intercalation time of cations into electroactive ZnO creates an additional opportunity to create fast response hybrid battery-supercapacitor Zn electrodes. Coloration efficiency of the ZnO material is competitive with the leading electrochromic materials, opening up ZnO as a promising alternative electrochromic material. Overall, these results improve the understanding of the physical mechanisms causing ZnO electroactivity, and knowledge of this phenomenon enables improved Zn battery performance and opens new possibilities for application of ZnO.

## 4. Materials and Methods

*UV-vis spectroscopy*: Electroactive ZnO was generated *in situ* on a 5 mm by 5 mm Zn foil electrode positioned at a 45° angle coincident to the illumination windows in a UV-vis cuvette. An Ocean Optics DH-mini UV-Vis-NIR Light source with deuterium and halogen lamp was used as a light source, and a Gamry Spectro-115U UV-vis spectrometer was used to collect operando UV-vis spectra in a reflection geometry. Further information can be found in S.I. Section 6.

*Impedance spectroscopy for ZnO conductivity measurements*: Electroactive ZnO was generated on a 0.25 mm thick Zn metal foil electrode contacted with two copper wires spaced 0.67 mm apart. Zn converted to electroactive ZnO, and the copper wires were observed to be in contact only with the electroactive ZnO. Chronoamperometry was performed on the Zn/ZnO electrode to control the electrochemical potential of the ZnO. Simultaneously, impedance spectroscopy was performed on the ZnO via the copper wires with a second potentiostat. Impedance spectroscopy measurements were taken between 150 kHz and 1 Hz. Further information can be found in S.I. Section 9.

*Discharge of Zn-alkaline batteries*: The Zn-alkaline batteries for operando optical microscopy was constructed using commercial battery materials including a Zn electrode, cellophane separator, electrolytic $MnO_2$ provided by Urban Electric Power (UEP) or NiOOH provided by HighStar Battery Company of China. For the cell of Figure 1, we constructed Zn vs. NiOOH batteries with Zn reference electrodes, excess NiOOH, and a high Zn areal mass loading of 185

mg/cm$^2$. We discharged the batteries at a fast rate of 125 mA/g$_{Zn}$ until a voltage limit or a capacity limit of 50% of the theoretical capacity of the Zn (410 mAh/g) was reached. In one test, the electrode voltage limit was set to 0.17 V vs. Zn/$Zn^{2+}$, and in another test the voltage limit was set to 0.6 V vs. Zn/$Zn^{2+}$. Once the voltage limit was reached, constant voltage discharge was sustained until current reduced to a trickle or the capacity limit was reached, and then the battery was recharged and discharge repeated. For the cell in Figure 3, four $MnO_2$ electrodes were used in cell construction to make the Zn limited in capacity compared to $MnO_2$, and electrodes were cut to 1 cm x 2 cm for the operando optical microscopy cell. The battery was galvanostatically discharged in 5.5 M KOH electrolyte. When the Zn electrode potential measured 1.25 V, the discharge step stopped, and the cell was allowed to relax to OCV.

Cell housings were constructed using J-B Weld Clearweld, Devcon 5-minute Epoxy Gel, poly(methyl methacrylate), Thermo Scientific plain microscope slides, and Thermo scientific Microscope Cover Glass No. 1 Thickness, purchased from McMaster Carr. A glass viewing window was built into the cell housing for operando optical microscopy. A 10x objective on a BX51RF Olympus microscope was used for data acquisition. To generate the in-focus images in the figures and videos, homemade software was used to control a stepper motor and camera to collect 10 partially in-focus images at different depths then stitch the images together into one fully in-focus image.

*Synchrotron X-Ray diffraction*: Electroactive ZnO was generated on a 0.05 mm thick Zn metal foil electrode. XRD measurements were then taken on the electroactive ZnO at selected potentials between 0.05 V and 1.5 V. Zn electrode potential was then held at 0.5 V for 14 hours until layer of amber ZnO was visible with an optical microscope. XRD measurements were then taken on the amber ZnO. XRD Measurements were taken using 15 keV X-rays from the 5-ID SRX beamline at National Synchrotron Light Source II at Brookhaven National Laboratory. Further information can be found in S.I. Section 10.

*Nuclear magnetic resonance spectroscopy* (NMR): Solid-state $^1$H and $^{23}$Na MAS NMR measurements were acquired on a 14.1 T narrow-bore superconducting magnet operating at 600.130 MHz for $^1$H and 158.748 MHz for $^{23}$Na. A PhoenixNMR 1.6-mm HXY MAS probehead was used for all experiments, which were conducted under MAS at spin rates of 10 kHz for $^1$H or

30 kHz for $^{23}$Na. Sample temperatures were maintained 283.0 K for $^{1}$H measurements and 293.1 K for $^{23}$Na measurements unless otherwise noted by providing temperature-controlled air to the probehead at 600 L/h for the duration of testing. $^{1}$H shifts were referenced to adamantane at 1.8 ppm. $^{23}$Na shifts were referenced to 1 M NaCl in $H_2O$ at 0 ppm.

Quantitative $^{23}$Na single-pulse measurements were acquired with $\pi/6$ radio frequency (rf) pulses of 0.617 μs (rf field strength of 1.64 MHz) and a recycle delay of 0.1 s. Quantitative $^{1}$H single-pulse measurements were acquired with $\pi/2$ rf pulses of 1.45 μs (rf field strength of 670 kHz) and a recycle delay of 30 s. Quantitative Hahn spin-echo measurements were acquired with a single rotor period (100 μs) delay between the $\pi/2$ and $\pi$ pulses. Sample preparation information can be found in S.I. Section 11.

*Chemical reduction and intercalation*: Procedures similar to Valdez et al. were followed. All chemicals were obtained from Sigma Aldrich or Fisher Scientific and used as received. All work was performed in a glovebox under argon atmosphere. Electroactive ZnO was placed in 2 mL of a 1:1 v/v mixture of tetrahydrofuran (THF) and toluene. A stoichiometric excess of one salt from the set [$LiBF_4$, NaTFSI, KTFSI, CsCl] was then dissolved into the solution by stirring. Finally, a stoichiometric excess of bis(pentamethylcyclopentadienyl) cobalt(II) ($CoCp^*_2$) was stirred into the same mixture to cause the redox reduction reaction to go forward and convert the electrochemical ZnO to deep blue. A control experiment of only $CoCp^*_2$ with the electrochromic ZnO in THF:toluene caused minimal color change to the ZnO. Classical ZnO did not change color at all with any combination of these ingredients.

*X-Ray Fluorescence (XRF)*: XRF measurements were performed with a Bruker M4 Tornado micro XRF spectrometer with a 25 μm spot size, a 40 kV tube voltage, a 600 μA tube current, and a 1-hour measurement time. Sample preparation information can be found in S.I. Section 13.

*Photoluminescence*: Photoluminescence studies were carried out on an Olympus IX83 inverted microscope coupled to a Princeton Instruments spectrometer with a PIXIS 1024B EMCCD camera. A 325nm He-Cd laser passing through a 400nm short-pass filter was used for sample excitation through an Olympus 20x objective. The photoluminescence was collected by the same objective and passed through to the monochromator.

*Confocal Raman spectroscopy*: Confocal Raman spectroscopy measurements were taken on ZnO generated in 5.5 M potassium hydroxide electrolyte previously saturated with ZnO. Electroactive ZnO was generated on a 0.25 mm thick Zn metal foil electrode by holding electrode potential 0.2 V above Zn equilibrium. Amber ZnO was generated by holding electrode potential 0.5 V above Zn equilibrium for 12 hours until a layer of amber ZnO accumulated. A WITec alpha300R Confocal Raman Microscope with A 50X: Zeiss EC Epiplan, NA 0.75 HD objective was used to obtain measurements of the ZnO accumulated on a Zn foil electrode. For the presented data, either a 532 nm laser at ~1 mW or a 633 nm laser at ~5 mW was used. 300 acquisitions of 1 second each were taken and signal averaged. A Princeton Advanced Research Versastat 4 was used to control potential.

## Notes

The authors declare no competing financial or non-financial interests.


## Acknowledgements

The authors thank Professor Alexander Couzis and Professor Stephen O'Brien for discussions, Ms. Julia Dacanay and Mr. Ayoub Diouri for device preparation, Dr. Rahul Deshmukh and Professor Vinod Menon for the photoluminescence spectrum. This work was supported by the U.S. Department of Energy, Office of Electricity, Energy Storage program through a contract from Sandia National Laboratories. Sandia National Laboratories is a multi-program laboratory managed and operated by National Technology and Engineering Solutions of Sandia, LLC., a wholly owned subsidiary of Honeywell International, Inc., for the U.S. Department of Energy's National Nuclear Security Administration under contract DE-NA-0003525. The views expressed herein do not necessarily represent the views of the U.S. Department of Energy or the United States Government. This research used 5-ID SRX of the National Synchrotron Light Source II, a U.S. Department of Energy (DOE) Office of Science User Facility operated for the DOE Office of Science by Brookhaven National Laboratory under Contract No. DE-SC0012704.


## Author Contributions

B.E.H. and D.E.T. conceived the ideas, designed and conducted experiments, analyzed and interpreted the data, and drafted the manuscript. R.J.M. led solid-state NMR measurements and helped edit the manuscript. G.G.Y. and S.B. contributed to conception and interpretation of the work. A.M.K. created hardware, software, and experimental methods enabling use of beamline 5-ID at Brookhaven Nation Laboratory's NSLS-II for XRD data acquisition. T.N.L. contributed to the conception of the work and conducted XRF experiments. *All authors approve of and account for all aspects of the submitted manuscript.*


[1] M. J. D'Ambrose, D. E. Turney, G. G. Yadav, M. Nyce, S. Banerjee, *ACS Appl. Energy Mater.* **2021**, *4*, 3381.

[2] D. E. Turney, J. W. Gallaway, G. G. Yadav, R. Ramirez, M. Nyce, S. Banerjee, Y. C. K. Chen-Wiegart, J. Wang, M. J. D'Ambrose, S. Kolhekar, J. Huang, X. Wei, *Chem. Mater.* **2017**, *29*, 4819.

[3] F. R. McLarnon, E. J. Cairns, *J. Electrochem. Soc.* **1991**, *138*, 645.

[4] N. D. Ingale, J. W. Gallaway, M. Nyce, A. Couzis, S. Banerjee, *J. Power Sources.* **2015**, *276*, 7.

[5] K. Ellmer, A. Klein, B. Rech, *Transparent conductive zinc oxide: basics and applications in thin film solar cells (Vol. 104)*, Springer Science & Business Media, **2007**.

[6] R. J. Mortimer, D. R. Rosseinsky, & P. M. Monk, *Electrochromic materials and devices*, John Wiley & Sons, **2015**.

[7] A. Janotti, C. G. Van De Walle, *Reports Prog. Phys.* **2009**, *72*.

[8] D. M. Bagnall, Y. F. Chen, Z. Zhu, T. Yao. S. Koyama, M. Y. Shen, T. Goto, *Appl. Phys. Lett.* **1997**, *70*, 2230.

[9] J. N. Schrauben, R. Hayoun, C. N. Valdez, M. Braten, L. Fridley, J. M. Mayer, *Science* **2012**, *336*, 1298.

[10] A. Valdés, J. Brillet, M. Grätzel, H. Gudmundsdóttir, H. A. Hansen, H. Jónsson, P. Klüpfel, G. J. Kroes, F. Le Formal, I. C. Man, R. S. Martins, J. K. Nørskov, J. Rossmeisl, K. Sivula, A. Vojvodic, M. Zäch, *Phys. Chem. Chem. Phys.* **2012**, *14*, 49.

[11] M. Bockelmann, L. Reining, U. Kunz, T. Turek, *Electrochim. Acta*, **2017**, *237*, 276-298.

[12] R. W. Powers, *J. Electrochem. Soc.* **1971**, *118*, 685.

[13] R. W. Powers and M. W. Breiter. *J. Electrochem. Soc.* **1969**, *116*, 719.

[14] M. C. H. McKubre, D. D. Macdonald, *J. Electrochem. Soc.* **1981**, *128*, 524.

[15] Q. C. Horn, Y. Shao-Horn, *J. Electrochem. Soc.* **2003**, *150*, A652.

[16] I. Arise, S. Kawai, Y. Fukunaka, and F. R. McLarnon. *J. Electrochem. Soc.* **2012**, *160*, D66.

[17] J. F. Parker, C. N. Chervin, I. R. Pala, M. Machler, M. F. Burz, J. W. Long, D. R. Rolison, *Science*, **2017** *356*, 415.

[18] F. Wang, O. Borodin, T. Gao, X. Fan, W. Sun, F. Han, A. Faraone, J. A. Dura, K. Xu, C. Wang, *Nat. Mater.* **2018**, *17*, 543.

[19] G. G. Yadav, J. Cho, D. Turney, B. Hawkins, X. Wei, J. Huang, S. Banerjee, M. Nyce, *Adv. Energy Mater.* **2019**, *9*.

[20] V. Srikant, D. R. Clarke, *J. Appl. Phys.* **1998**, *83*, 5447.

[21] a) G. W. Tomlins, J. L. Routbort, T. O. Mason *J. Appl. Phys.* **2000**, *87*(1), 117; b) K. Ellmer, *J. Phys. D. Appl. Phys.* **2001**, *34*, 3097; c) P. H. Miller, *Phys. Rev.* **1941**, *60*, 890.

[22] T. Izumi, K. Izumi, N. Kuroiwa, A. Senjuh, A. Fujimoto, M. Adachi, T. Yamamoto, *J. Alloys Compd.* **2009**, *480*, 123.

[23] C. N. Valdez, M. F. Delley, J. M. Mayer, *J. Am. Chem. Soc.* **2018**, *140*, 8924.

[24] W. Wu, M. Wang, J. Ma, Y. Cao, Y. Deng, *Adv. Elec. Mater.* **2018**, *4*, 1800185.

[25] X. Zhang *Corrosion and Electrochemistry of Zinc* Springer Science, Toronto **1996**.

[26] G. Davies, A. G. Hsieh, M. Hultmark, M. E. Mueller, D. A. Steingart, *J. Electrochem. Soc.* 2016, *163*, A1340.

[27] Y. Shen, K. Kordesch, *J. Power Sources.* **2000**, *87*, 162.

[28] H. Yang, *J. Power Sources.* **2004**, *128*, 97.

[29] P. M. Monk, R. J. Mortimer, D. R. Rosseinsky *Electrochromism: fundamentals and applications* John Wiley & Sons, **2008**.

[30] M. N. Hull, J. E. Ellison, J. E. Toni, *J. Electrochem. Soc.* **1970**, *117*, 192.

[31] E. Faegh, T. Omasta, M. Hull, S. Ferrin, S. Shrestha, J. Lechman, D. Bolintineanu, M. Zuraw, W. E. Mustain, *J. Electrochem. Soc.*, **2018**, *165*, A2528.

[32] P. Kubelka, F. Munk, *Z. Tech. Phys.* **1931**, *12*, 593.

[33] E. Burstein, *Phys. Rev.* **1954**, *93*, 632.

[34] J. G. Lu, S. Fujita, T. Kawaharamura, H. Nishinaka, Y. Kamada, T. Ohshima, Z. Z. Ye, Y. J. Zeng, Y. Z. Zhang, L. P. Zhu, H. P. He, B. H. Zhao, *J. Appl. Phys.* **2007**, *101*.

[35] T. Pisarkiewicz, K. Zakrzewska, E. Leja, *Thin Solid Films.* **1989**, *174*, 217

[36] K. Ellmer, *J. Phys. D. Appl. Phys.* **2001**, *34*, 3097.

[37] J. R. Bellingham, W. A. Phillips, C. J. Adkins, *J. Mater. Sci. Lett.* **1992**, *11*, 263.

[38] T. Minami, H. Sato, K. Ohashi, T. Tomofuji, S. Takata, *J. Cryst. Growth* **1992**, *117*, 370.

[39] H. Peelaers, C. G. Van De Walle, *Phys. Rev. B* **2019**, *100*, 81202.

[40] H. Peelaers, E. Kioupakis, C. G. Van De Walle, *Phys. Rev. B - Condens. Matter Mater. Phys.* **2015**, *92*.

[41] H. Peelaers, E. Kioupakis, C. G. Van De Walle, *Appl. Phys. Lett.* **2012**, *100*, 1.

[42] C. Y. Tsai, *IEEE J. Sel. Top. Quantum Electron.* **2020**, *26*.

[43] W. Wang, H. Peelaers, J. X. Shen, C. G. Van De Walle, *MRS Commun.* **2018**, *8*, 926.

[44] A. M. Schimpf, N. Thakkar, C. E. Gunthardt, D. J. Masiello, D. R. Gamelin, *ACS Nano* **2014**, *8*, 1065.

[45] M. A. Scibioh and B. Viswanathan, Materials for Supercapacitor Applications, Elsevier, **2020.**

[46] A. Sawa, *Mat. Today* **2008**, *11*, 28.

[47] N. Lu, P. Zhang, Q. Zhang, R. Qiao, Q. He, H. B. Li, Y. Wang, J. Guo, D. Zhang, Z. Duan, Z. Li, M. Wang, S. Yang, M. Yan, E. Arenholz, S. Zhou, W. Yang, L. Gu, C. W. Nan, J. Wu, Y. Tokura, P. Yu, *Nature* **2017**, *546*, 124.

[48] M. A. Hope, K. J. Griffith, B. Cui, F. Gao, S. E. Dutton, S. S. P. Parkin, C. P. Grey, *J. Am. Chem. Soc.* **2018**, *140*, 16685.

[49] S. Ghosh, J. Castillo-Lora, A. V. Soudackov, J. M. Mayer, S. Hammes-Schiffer, *Nano Lett.* **2017**, *17*, 5762.

[50] C. N. Valdez, A. M. Schimpf, D. R. Gamelin, J. M. Mayer, *J. Am. Chem. Soc.* **2016**, *138*, 1377.

[51] A. M. Schimpf, C. E. Gunthardt, J. D. Rinehart, J. M. Mayer, D. R. Gamelin, *J. Am. Chem. Soc.* **2013**, *135*, 16569.

[52] C. N. Valdez, M. F. Delley, J. M. Mayer, *J. Am. Chem. Soc.* **2018**, *140*, 8924.

[53] F. A. Selim, M. H. Weber, D. Solodovnikov, K. G. Lynn, *Phys. Rev. Lett.* **2007**, *99*, 1.

[54] M. H. Weber, N. S. Parmar, K. A. Jones, K. G. Lynn, *J. Electron. Mater.* **2010**, *39*, 573.

[55] L. E. Halliburton, N. C. Giles, N. Y. Garces, M. Luo, C. Xu, L. Bai, L. A. Boatner, *Appl. Phys. Lett.* **2005**, *87*, 1.

[56] M. Wang, G. Yu, W. Ji, L. Li, W. Ding, L. Peng *Chem. Phys. Lett.* **2015,** *627*, 7-12.

[57] T. Li, M. Wang, X. Liu, M. Jin, F. Huang. *Phys. Chem. Lett.* **2020** *11*(7), 2402-2407.

[58] L. Q. Wang, X. D. Zhou, G. J. Exarhos, L. R. Pederson, C. Wang, C. F. Windisch Jr, C. Yao. *App. Phys. Lett.* **2007** *91*(17), 173107.

[59] R. J. Messinger, M. Ménétrier, E. Salager, A. Boulineau, M. Duttine, D. Carlier, J. M. Ateba Mba, L. Croguennec, C. Masquelier, D. Massiot, M. Deschamps, *Chem. Mater*, **2015**, *27*, 5212.

[60] N. Uekawa, R. Yamashita, Y. J. Wu, K. Kakegawa, *Phys. Chem. Chem. Phys.* **2004**, *6*, 442.

[61] M. V. Klein, S. P. S. Porto, *Phys. Rev. Lett.* **1969**, *22*, 782.

[62] J. F. Scott, *Solid State Commun.* **1971**, *9*, 759.

[63] a) D. Banerjee, J. Y. Lao, D. Z. Wang, J. Y. Huang, D. Steeves, B. Kimball, Z. F. Ren, *Nanotechnology*, **2004**, *15*, 404; b) K. Vanheusden, C. H. Seager, W. L. Warren, D. R. Tallant, J. A. Voigt, *Appl. Phys. Lett.* **1996**, *68*, 403; c) K. Vanheusden, W. L. Warren, C. H. Seager, D. R. Tallant, J. A. Voigt, B. E. Gnade, *J. Appl. Phys.* **1996**, *79*, 7983; d) G. Heiland, E. Mollwo, F. Stöckmann, *Solid State Phys. - Adv. Res. Appl.* **1959**, *8*, 191.

[64] W. B. Cai, D. A. Scherson, *J. Electrochem. Soc.* **2003**, *150*, B217.

[65] C. F. Windisch, G. J. Exarhos, C. Yao, L. Q. Wang, *J. Appl. Phys.* **2007**, *101*.

[66] X. Xue, T. Wang, X. Jiang, J. Jiang, C. Pan, Y. Wu, *CrystEngComm* **2014**, *16*, 1207.

[67] X. Wang, Q. Li, Z. Liu, J. Zhang, Z. Liu, R. Wang, *Appl. Phys. Lett.* **2004**, *84*, 4941.

[68] Z. Q. Chen, A. Kawasuso, Y. Xu, H. Naramoto, X. L. Yuan, T. Sekiguchi, R. Suzuki, T. Ohdaira, *J. Appl. Phys.* **2005**, *97*, 1.

[69] S. Hussain, Y. Khan, V. Khranovskyy, R. Muhammad, R. Yakimova, *Prog. Nat. Sci. Mater. Int.* **2013**, *23*, 44.

[70] J. Fang, H. Fan, Y. Ma, Z. Wang, Q. Chang, *Appl. Surf. Sci.* **2015**, *332*, 47.

[71] A. Janotti, C. G. Van de Walle, *Appl. Phys. Lett.*, **2005**, *87*, 122102.

[72] A. Janotti, C. G. Van de Walle, *Nat. Mat.*, **2007**, *6*, 44.